https://doi.org/10.1016/j.apenergy.2018.05.015

Full Paper

Nitrogen-doped graphene derived from ionic liquid as metal-free catalyst for oxygen reduction reaction and its mechanisms

*Yiyi She [a,c], Jinfan Chen [b], Chengxu Zhang [a,d], Zhouguang Lu [e], Meng Ni [f], Patrick H.-L. Sit [b], Michael K.H. Leung [a,b,c] **

[a] *Ability R&D Energy Research Centre, School of Energy and Environment, City University of Hong Kong, Hong Kong, China*
[b] *School of Energy and Environment, City University of Hong Kong, Hong Kong, China*
[c] *City University of Hong Kong Shenzhen Research Institute, Shenzhen, Guangdong, China*
[d] *The Engineering Laboratory of Advanced Battery and Materials of Yunnan Province, Faculty of Metallurgical and Energy Engineering, Kunming University of Science and Technology, Kunming, China*
[e] *Department of Materials Science and Engineering, South University of Science and Technology of China, Shenzhen, Guangdong, 518055, China*
[f] *Department of Building and Real Estate, The Hong Kong Polytechnic University, Hong Kong, China*

Abstract

It is of great significance to develop N-doped carbon materials possessing high catalytic activity, excellent durability and low cost for oxygen reduction reaction (ORR) due to imperative for energy devices with high energy density, such as fuel cells and metal-air batteries. Herein, N-doped graphene is prepared by annealing a homogeneous mixture of graphene oxide (GO) and ionic liquid of 1-butyl-3-methylimidazolium tetrafluoroborate ([Bmim]BF_4) in N_2 atmosphere. By entrapping effect, the ionic liquid serves as both N source and restacking protectant in formation of high-quality N-doped graphene sheets. Electrochemical characterizations reveal that the obtained N-doped graphene possesses excellent electro-catalytic properties for ORR in alkaline condition with onset potential of -39 mV (vs. Hg/HgO) and current density of 5.83 mA cm^{-2} at -0.9 V (vs. Hg/HgO) at 2500 rpm. The microstructure of the prepared catalysts and their ORR catalytic activities are highly sensitive to calcination temperature and the optimal temperature is 900 ^oC. Density functional theory (DFT) analysis indicates from the atomic point of view that N atoms with different

* Corresponding author. Tel: +852 3442 4626; Fax: +852 3442 0688; E-mail address: mkh.leung@cityu.edu.hk

The short version of the paper was presented at ICAE2017, Aug 21-24, Cardiff, UK. This paper is a substantial extension of the short version of the conference paper.

configurations contribute unequally to the ORR performance enhancement. Pyridinic N at the edge of graphene plays the most significant role in improving ORR performance owing to the largest number of active sites and lower band gap. Based on the experimental and simulation results, the beneficial properties of the as-prepared N-doped graphene for ORR are ascribed to the superior conductivity of graphene, the high N doping content and the high proportion of active pyridinic N species.

Keywords: Density functional theory; Fuel cell; Heteroatom doping; Metal-air battery; Metal-free catalyst.

* Corresponding author. Tel: +852 3442 4626; Fax: +852 3442 0688; E-mail address: mkh.leung@cityu.edu.hk

The short version of the paper was presented at ICAE2017, Aug 21-24, Cardiff, UK. This paper is a substantial extension of the short version of the conference paper.

1. Introduction

The ever-growing global energy demand and the mission of environmental protection have promoted the exploration of renewable energy storage and conversion technologies [1, 2], among which fuel cell and metal-air battery show great prospect owing to high energy density and environmental friendliness [3-5]. However, their wide application is severely hampered by the sluggish reaction kinetics of oxygen reduction reaction (ORR) on cathode, requiring high loading of Pt catalysts to maintain the performance of energy devices [6, 7]. In the past few decades, extensive efforts have been devoted to explore advanced noble metal-free catalysts in order to improve ORR catalytic activity and lower the cost [8]. Among all potential candidates, heteroatom-doped (such as B, N, S and P) carbon materials, especially heteroatom-doped graphene, have attracted great research attention due to intrinsic merits of graphene, low fabrication cost and remarkable ORR catalytic activity [9-13]. The mechanism concerning heteroatom-doped carbon materials for ORR performance enhancement has been extensively discussed and evaluated by density functional theory (DFT) [14-16]. It is commonly considered that the reallocation of the electronic charge, induced by the electronegativity difference between carbon atoms and doped heteroatoms, creates positive-charged active sites and, thus, facilitates the O_2 adsorption in the ORR process [17]. Further DFT investigations have shown that the change of spin density, doping cluster size and dopant-defect interactions also play a significant role in ORR performance boost in addition to the change of charge density [18, 19]. It is noteworthy that these calculations regarding N-doped graphene, which is one of the most promising substitute for Pt catalyst, are exclusively based on substituting N atoms for C at the edge of graphene framework [20]. However, revealed by comprehensive experimental results, N-doped carbon materials consist of three effective N configurations for ORR in the carbon skeleton including pyridinic N, pyrrolic N and graphitic N, each of which could locate either inside or at the edge of graphene [21, 22].

Therefore, It is highly desirable for material design and mechanism exploration to figure out how each N configuration functions in ORR from the atomic point of view and which one is the most effective configuration.

For heteroatom doping, various heteroatom sources, such as ammonium, ethylenediamine, melamine, benzyl disulfide, polymer, etc., have been applied to fabricate heteroatom-doped carbon materials [23-27]. However, they are either flammable or toxic, resulting in hazards and environmental problems. Ionic liquids (ILs), defined as semi-organic salts existing in the liquid state below 100 ℃, were initially developed as molten electrolyte for electrochemical applications due to its excellent ion conductivity [28]. In recent years, there are more research interests in using ILs as precursors for fabricating heteroatom-doped carbon materials by carbonization method [10, 29, 30]. ILs with cross-linkable anions such as nitrile groups are regarded as favorable precursors of this application owing to the polymerization of cross-linkable groups at elevated temperature, giving higher carbon yield compared with conventional ILs [31, 32]. By an entrapping effect, ILs without cross-linkable groups have also been reported as precursors for the synthesis of heteroatom-doped carbon materials with the assistance of foreign frameworks [33, 34]. Compared with carbonizing pure ILs with cross-linkable groups, this strategy not only enables delicate morphology design, but also reduces fabrication cost. Particularly, when graphitic carbon framework is applied, the CH-π interaction between ILs and graphitic support facilitates the entrapping and directing of ILs into carbon skeleton [4, 35].

Herein, we report a simple strategy to synthesize high-quality N-doped graphene by annealing a homogeneous mixture of graphene oxide (GO) and conventional hydrophilic ionic liquid, 1-Butyl-3-methylimidazolium Tetrafluorobotate ([Bmim]BF_4). Being intrinsically charged, the [Bmim]BF_4 can be uniformly adsorbed on the surface of GO, serving as both N dopant and restacking protectant in the subsequent calcination process.

Moreover, the use of GO as foreign carbon framework eliminates template removal process which inevitably involves strong acid or alkaline, rendering it promising for large-scale production and improved environmental performance. The as-fabricated N-doped graphene shows remarkable electro-catalytic activity towards ORR in alkaline conditions with maximum current density of 6 mA cm^{-2}. The influence of calcination temperature on the microstructure and ORR catalytic activity is intensively investigated. The effect of each N configuration in graphene, inside or at the edge, on ORR performance is systematically calculated by DFT. This work not only presents a facial and scalable way to fabricate cost-effective catalysts for ORR, but also possesses high academic value in understanding its mechanisms.

2. Experimental

2.1. Synthesis of N-doped graphene

In a typical synthesis, GO was firstly prepared from graphite powder (Acros) according to a modified Hummers method [35, 36]. An amount of 20 mg of as-prepared GO was dispersed homogeneously in 20 mL deionized water by ultrasonication. Then 2 mL of [Bmim]BF_4 was dropped into the GO solution by pipette under stirring followed by adjusting the pH of the suspension to around 11 with diluted NaOH solution. The suspension was placed on a hotplate and heated at 120 ℃ under vigorous stirring until sticky carbon ink was obtained. Finally, the pasty mixture was transferred to a covered crucible and calcined in N_2 atmosphere at elevated temperature for 1 hour in a tube furnace (Carbolite HZS 12/600) with a heating rate of 5 ℃ min^{-1}. The samples after calcination were subjected to ORR electrochemical test without any post treatment.

2.2. Material characterization

The morphology and microstructure of the as-synthesized catalysts were characterized by scanning electron microscopy (SEM, JEOL JSM-6490) and transition electron microscopy (TEM, JEOL JEM 2100F). The surface chemical composition of samples was analyzed by X-ray photoelectron spectroscopy (XPS, PHI-5600) with Al Kα radiation (hν=1486.6 eV). The full and high-resolution spectra were recorded in step sizes of 0.5 eV and 0.1 eV, respectively, at a pass energy of 58.7 eV. All XPS spectra were corrected with respect to C 1s peak at 284.8 eV.

2.3. Electrochemical test

A traditional three-electrode system connected to a CHI 660 electrochemical testing system was applied to all the electrochemical tests in this paper. A glassy carbon electrode (GCE, diameter of 5 mm, PINE instruments, USA), a Pt foil and an Hg/HgO (1 M KOH) electrode were selected as the working, counter and reference electrodes, respectively. For the rotating disk electrode (RDE) experiment, a PINE rotator was used. Prior to coating, the surface of GCE was polished in sequence with 1.0, 0.3 and 0.05 μm alumina powders on a polishing cloth and rinsed with deionized water. An amount of 10 μL suspension of the as-prepared catalyst (or commercial 20 wt% Pt/C (Fuel Cell Earth LLC) as reference) in anhydrous ethanol (1 mg sample mL^{-1}) was subsequently dropped onto the polished surface of the GCE with a pipette and dried in air. This procedure was repeated for three times. Finally, 10 μL of Nafion solution (0.5 wt%) was coated onto the surface of modified GCE and dried in air before use. All electrolytes were purged with high purity N_2 or O_2 for 40 minutes prior to measurements. In the ORR experiments, the O_2 (or N_2) saturated condition was guaranteed by introducing constant O_2 (or N_2) gas flow above the surface of the electrolyte. All the

experiments were conducted at room temperature. The onset potential (E_{onset}) was deemed at which the current density was equal to -0.1 mA cm^{-2} after background subtraction.

Koutecky-Levich (K-L) equation given below was applied to calculate the electron transfer number per one oxygen molecule in the ORR process:

$$1/j = 1/j_k + 1/j_d = 1/j_k + 1/[0.62nF(D_{O2})^{2/3}\nu^{-1/6}C_{O2}\omega^{1/2}] \quad (1)$$

where j is the measured current density; j_k and j_d are the kinetic and diffusion limited current density, respectively; n is overall electron number transferred per oxygen molecule during ORR; F represents Faraday constant (96485 C mol^{-1}); D_{O2} is the diffusion coefficient of O_2 in the electrolyte (1.9×10^{-5} cm^2 s^{-1} in 0.1 M KOH); ν is kinematic viscosity of the electrolyte (0.01 cm^2 s^{-1}); C_{O2} is the bulk concentration of O_2 in the electrolyte (1.2×10^{-6} mol cm^{-3} in 0.1 M KOH); ω is rotating rate of the electrode (rad s^{-1}) [37].

3. Calculations

Spin-polarized density functional theory (DFT) calculations were performed to analyze the effect of different N configurations on the properties of the N-doped graphene and the corresponding impact on the ORR catalytic activity. Generalized gradient approximations functional (GGA), Perdew-Burke-Ernzerhof functional (PBE) [38] and ultrasoft pseudopotentials [39] were used in the calculations using the PWscf module of the Quantum Espresso package [40]. The gamma-point sampling was adopted and the plane-wave kinetic energy cutoffs for the wave functions and the charge density were chosen as 30 Ry and 240 Ry, respectively. In analyzing the atomic charges and spins, the Lowdin charges and spins were calculated. Six models of N-doped single-layer graphene with different doping configurations were built. C and N atoms on the edges of graphene were terminated by H atoms [18, 41, 42]. Each system was situated in a unit cell box for calculations. The side

length of the unit cell box was 30 Å, tested to be large enough for the effect of periodic boundary conditions to be negligible in the as-defined systems.

4. Results and discussion

4.1. Material characterization

In this synthesis, GO serves as the flake template. [Bmim]BF_4 is absorbed on the surface of GO spontaneously by electrostatic force. It protects the restacking of GO and decomposes to supply N in the calcination, in which doping and reducing are accomplished simultaneously. Four calcination temperatures of 700, 800, 900 and 1000 ℃ were chosen to synthesize NG700, NG800, NG900 and NG1000, respectively. For comparison, an undoped control sample (designated as UG) was also fabricated by the same procedure at 900 ℃ without adding [Bmim]BF_4.

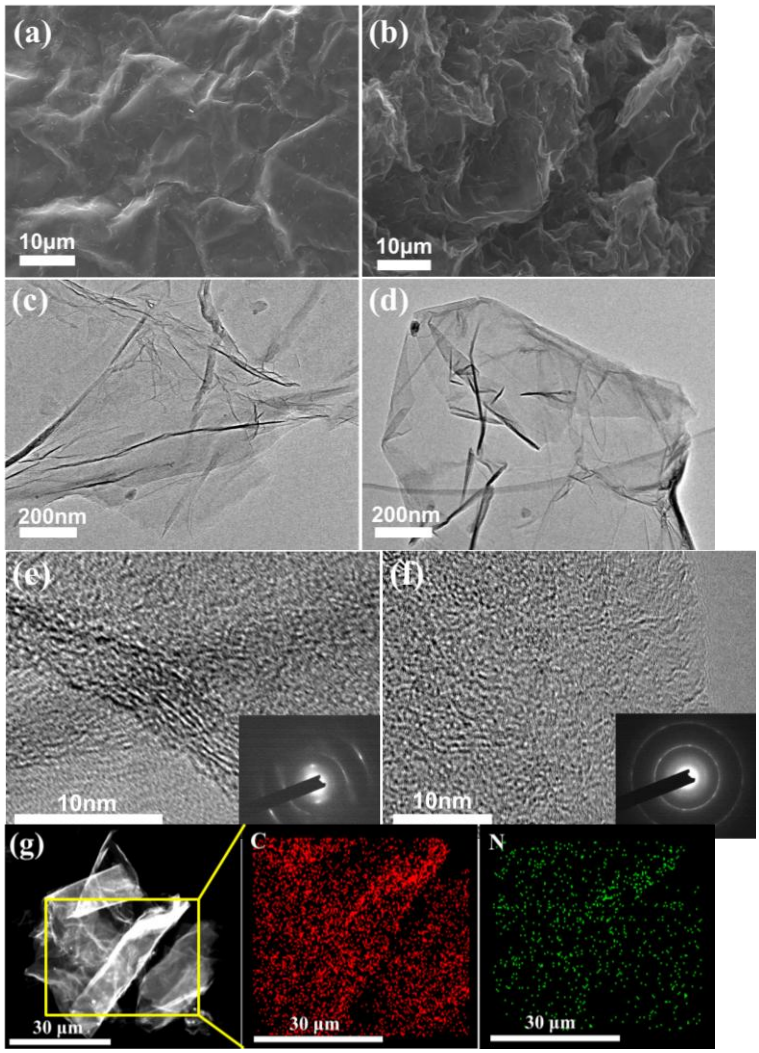

Fig. 1. SEM images of UG (a) and NG900 (b). TEM images of UG (c) and NG900 (d). HRTEM images of NG (e) and NG900 (f) with corresponding SAED patterns of area in image (e) and (f) as insets. Dark field TEM image of NG900 (g) and the elemental mapping images of the selected area in the square.

Figures 1(a) and 1(b) are typical SEM images of UG and NG900, respectively. The UG is severely restacked and shows thick plate morphology after calcination at 900 ℃, while NG900 displays more dispersed thin flakes due to the restacking protective function of [Bmim]BF_4 adsorbed on the surface of GO. The difference is further confirmed by TEM and HRTEM characterizations. Stacked thick layers and plenty of crumples are shown for UG without assistance of [Bmim]BF_4 (Fig. 1(c)) while transparent thin flakes are clearly observed for NG900 (Fig. 1(d)). In the edge area, NG900 is composed of quite thin multiple layers (Fig. 1(f)) while the layers of NG are much thicker and restacked (Fig. 1(e)). The corresponding

selected area electron diffraction (SAED) pattern indicates the polycrystalline nature of both NG900 and UG. However, despite the difference in thickness and smoothness, NG900 and NG share large similarity of morphology to GO, suggesting its function as template in this synthesis. Compared with the stacked UG, the much looser and thinner nanostructure of NG900 can facilitate the O_2 penetration, thus lower the energy barrier and facilitates the ORR process. The elemental mapping images (Fig. 1(g)) not only confirm the successful N doping, but also reveal its homogeneous distribution throughout the graphene sheets in NG900. For samples prepared under other temperatures, NG700 possesses poor electronic conductivity due to incomplete reduction of GO under this temperature (Figs. 2(a) and 2(b)). The typical morphology of NG800 having porous and thin flakes (Figs. 2(c) and 2(d)) are quite similar to NG900 as shown in Fig 1. NG1000 has more microfoldings and closer coupling among the graphene sheets for better thermodynamic stability owing to the interaction of van der waals at high temperature (Figs. 2(e) and 2(f)) [43].

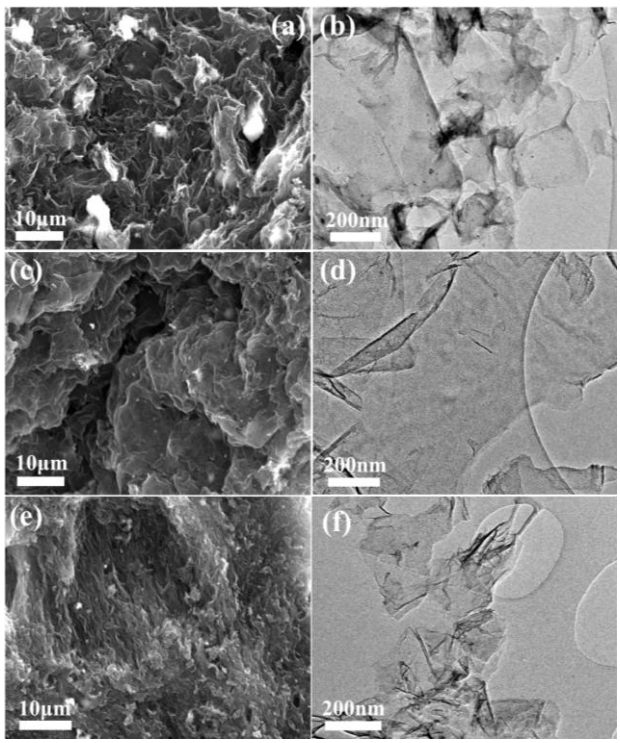

Fig. 2. SEM ((a), (c), (e)) and TEM ((b), (d), (f)) images of NG700 ((a), (b)) NG800 ((c), (d)) and NG1000 ((e), (f)).

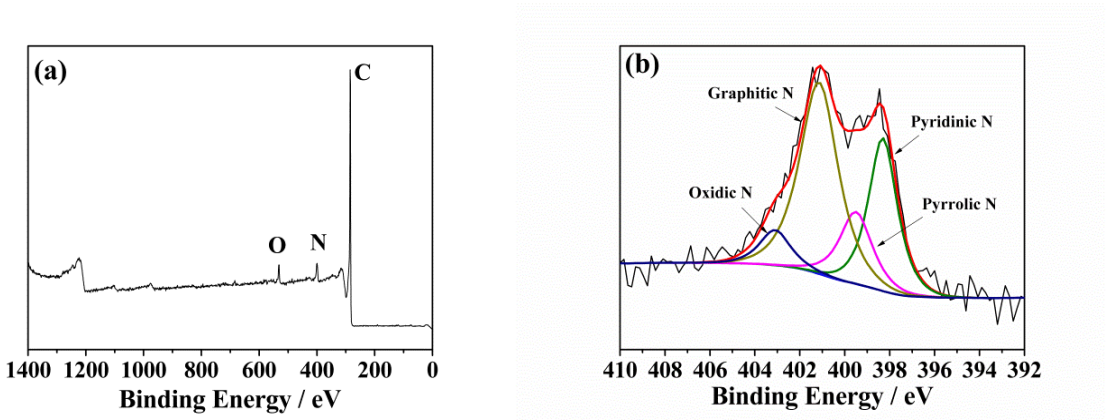

Fig. 3. Full (a) and high resolution N 1s (b) XPS spectra of NG900.

Table 1. N doping content and distribution of various N configurations obtained from the XPS results.

Samples	N content (at %)	Pyridinic N (at %) 398.4±0.1	Pyrrolic N (at %) 399.6±0.1	Graphitic N (at %) 401.1±0.1	Oxidic N (at %) 403.1±0.1
NG700	7.2	27.9	18.4	39.5	14.2
NG800	7.0	26.2	20.7	43.8	8.3
NG900	6.6	29.0	15.5	48.4	7.1
NG1000	4.9	33.5	8.6	51.6	6.3

XPS was conducted to reveal the surface chemical composition and the distribution of various N doping configurations. A peak of N which locates at around 400 eV is clearly seen in the full XPS spectrum of NG900 (Fig. 3(a)), further indicating the successful doping of N. No peak of F and B is observed probably because negative-charged GO is prone to be absorbed by positive-charged $[Bmim]^+$. High-resolution XPS spectra of N 1s of the samples prepared under different temperatures are presented in Fig. 3(b) and Fig. S1. All the spectra can be deconvoluted into four peaks, which correspond to pyridinic N (~398.4 eV), pyrrolic N (~399.6 eV), graphitic N (~401.1 eV) and oxidic N (~403.1 eV) [21, 44, 45]. The N doping content and the distribution of various N configurations derived from the ratio of deconvoluted peaks area after background subtraction are summarized in Table 1. It is noteworthy that the N doping content decreases from 7.2% to 4.9% as temperature increases

from 700 ℃ to 1000 ℃, suggesting that the N dopant is unstable and has a chance to be removed at elevated temperature [46, 47]. Moreover, the percentage of each N configuration in the overall N content varies according to different calcination temperatures. As the temperature increases, the percentages of graphitic N and pyridinic N increase accordingly while oxidic N and pyrrolic N decrease due to the instability of N-oxide and the five-membered heterocyclic rings. This is well consistent with the fact that pyridinic N is more stable than pyrrolic N but both tend to transform to graphitic N at high temperature [48]. High-resolution C 1s XPS spectra of samples under different temperatures are also shown in Fig. S2. The fitted peak locating at 285.9 eV is attributed to aromatic C-N bonds, reflecting successful doping of N into graphene again [45]. Distribution of various C configurations is summarized in Table S1 accordingly. The content of C-N in different samples estimated by multiplication of C content and C-N percentage decreases with increasing annealing temperature, which is in accordance with the change tendency of N content.

4.2. Electro-catalytic performance towards oxygen reduction reaction (ORR)

The ORR electro-catalytic activity of the as-prepared samples was investigated in 0.1 M KOH using a traditional three-electrode system. As can be seen in the cyclic voltammograms (CVs) (Fig. 4(a)), an obvious oxygen reduction peak appears at -0.18 V (vs. Hg/HgO) in the negative sweep of NG900, which is 0.17 V positive-shifted compared with UG. Moreover, the peak current density of NG900 is twice as large as that of UG, suggesting its superior ORR catalytic activity. Similar results were observed in linear sweep voltammograms (LSVs) (Fig. 4(b)), which were recorded by a rotating disk electrode at a rotational rate of 2500 rpm. Although the effect is not as distinguished as Pt catalyst, the onset potential and the current density are remarkably improved after N doping. For NG900, the ORR initiates at a potential of -39 mV (vs. Hg/HgO), much positive than UG and samples under other temperatures. The

current density of NG900 reaches 5.83 mA cm^{-2} at -0.9 V (vs. Hg/HgO) at 2500 rpm. In addition to N doping, the thinner and looser microstructure of NG900 also contributes to the ORR performance enhancement by facilitating O_2 penetration and providing larger contact area. Calcination temperature in synthesis has significant influence on ORR catalytic activity. NG700 exhibits the lowest current density and the most negative onset potential due to the unsatisfactory electronic conductivity resulting from incomplete reduction of GO in calcination at this temperature. Moreover, as indicated in Table 1, although the N doping content of NG700 is as high as 7.2 at%, 14.2 at% of it is in the form of oxidic N, which is regarded as an ineffective N doping moiety for ORR [49]. NG800 and NG1000 show similar catalytic performance with more positive onset potential for NG800 and slightly larger current density for NG1000. NG900 yields the largest current density and the most positive onset potential among all the catalysts. Owing to the similarity of NG800 and NG900 in morphology, the superior ORR catalytic activity of NG900 may result from a more effective composition of N configurations, to be discussed in detail in the following content. The inferior performance of NG1000 can be attributed to either the low N doping content or the destroyed thin flake morphology at high temperature, resulting in poor O_2 adsorption and penetration.

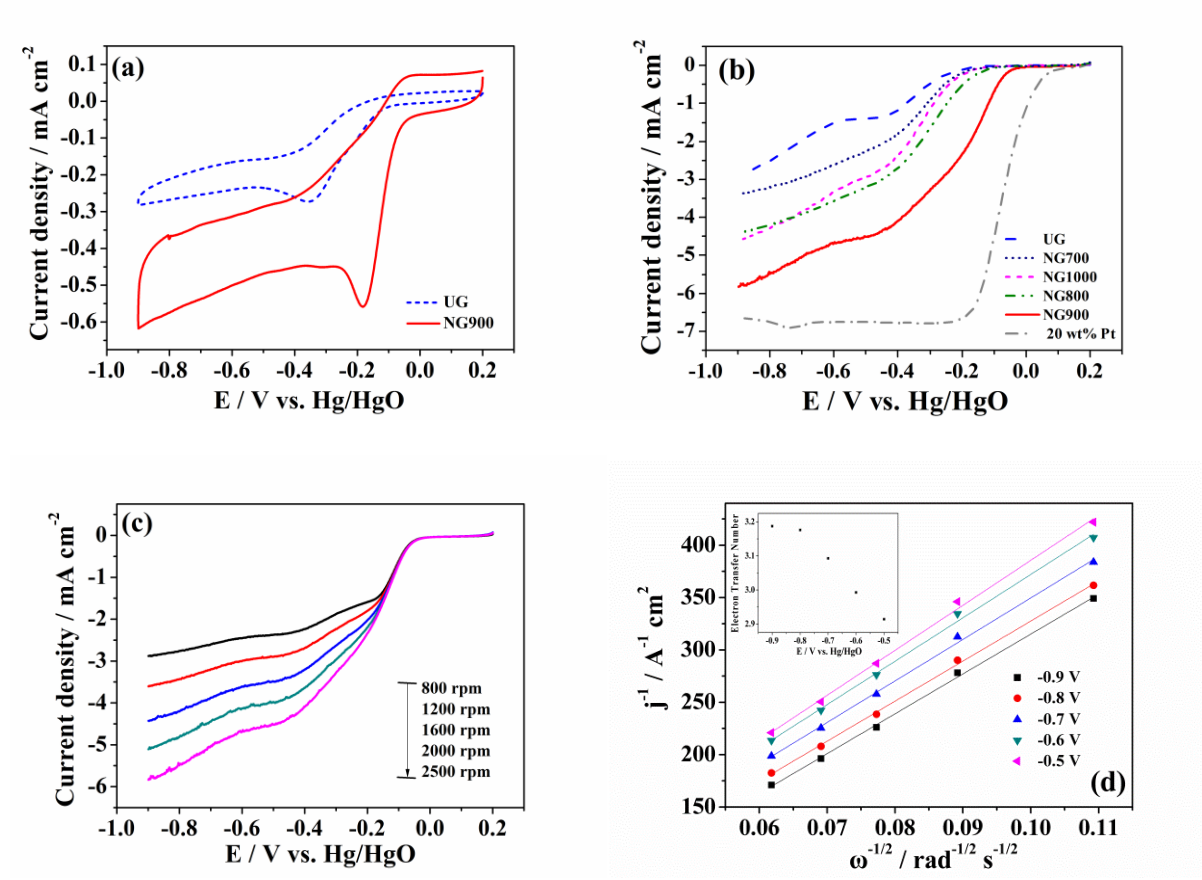

Fig. 4. (a) CVs of UG and NG900. (b) LSVs of different samples at rotational rate of 2500 rpm. (c) LSVs of NG900 at different rotational rates. (d) K-L plots of NG900 from -0.5 to -0.9 V; Inset: Electron transfer number determined by the K-L plots at corresponding voltages. Electrolyte: O_2-saturated 0.1 M KOH; Scan rate: 10 mV s^{-1}.

LSVs at different rotational speed were also recorded to reveal the ORR kinetics on various catalysts (Fig. 4(c) and Fig. S4). For both NG900 and UG, the current density increases with increasing rotational rate due to higher oxygen flux to the surface of the electrode. The corresponding Koutecky-Levich (K-L) plots (Fig. 4(d) and Fig. S5(a)) reflect good linear relationship between the reciprocal of current density and the reciprocal of the square root of the rotational rate in the voltage range from -0.5 to -0.9 V, indicating the first-order reaction kinetics towards the concentration of dissolved oxygen on both UG and NG900 [42]. However, based on the K-L equation, the electron transfer number of NG900 is calculated as 3.19 while the value of UG is only 1.69 at -0.9 V (vs. Hg/HgO) (Fig. 3(d) and

Fig. S5(b)), indicating that the ORR goes through a mixture of four-electron and two-electron process on NG900 while only two-electron pathway occurs on UG.

Since fuel crossover from anode to cathode is unavoidable in direct liquid fuel cell, the catalytic selectivity is vitally important for efficient ORR catalysts on cathode. A small quantity of 3 M methanol was introduced at 120th s in chronoamperometric (CA) measurement (Fig. 5(a)). The reversion in current density on commercial Pt catalyst upon the addition of methanol indicates the occurrence of methanol oxidation. In contrast, the current density of NG900 remains unchanged during the whole test, suggesting its excellent ORR catalytic selectivity.

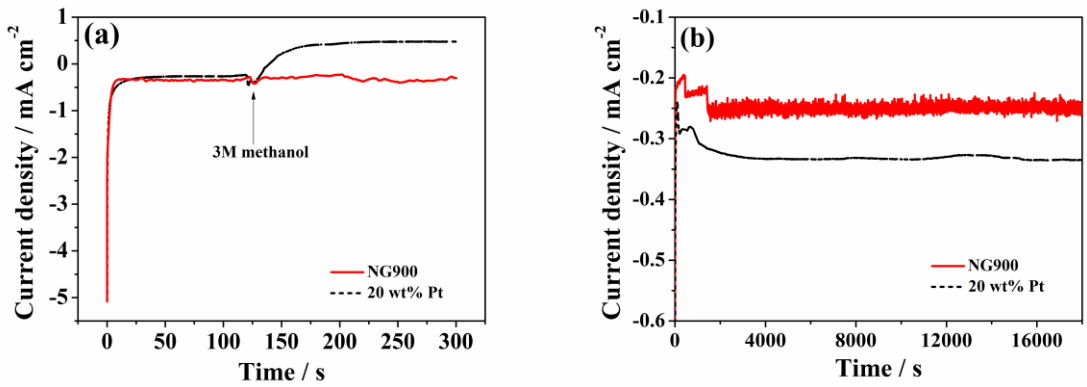

Fig. 5. Chronoamperometric (a) and I-t curves (b) of NG900 compared with commercial 20 wt% Pt at -0.2 V (vs. Hg/HgO) in O_2-saturated 0.1 M KOH.

The durability of NG900 and Pt catalysts was also investigated by I-t measurement (Fig. 5(b)) and CV test (Fig. S6). Continuous O_2 reduction for 5 hours on NG900 causes negligible loss of current density, implying its remarkable durability and potential application in alkaline fuel cell and metal-air battery.

ORR catalytic activity of N-doped graphene synthesized by three representative methods are compared in Table 2. Calcination at 800 ~ 1000 °C is necessary for superior ORR

catalysts since samples fabricated by wet hydrothermal method at low temperature exhibit modest performances even little amount of Fe is included [50]. Hard template and chemical vapor deposition (CVD) are effective ways to improve ORR catalytic activity by enlarging specific surface area, thus create more active sites which O_2 can get access to [51, 52]. However, they either need strong acid and alkaline to remove the template, or require complex equipment to fulfill the fabrication, which prevents their large-scale application considering cost and environmental issues. For our work, although onset potential and current density need further improvement, we present an extremely facile and green way to synthesize metal-free N-doped graphene with high N doping content and outstanding durability.

Table 2. Comparison of reported ORR performance of N-doped graphene in 0.1 M KOH.

Doping treatment	Precursor	N content (at.%)	Template/ removal method	E^{a}_{Onset} (V vs. RHE)	Current density[b] (mA cm^{-2})	Durability (retention %)	Ref.
Hydrothermal method	GO, dicyandiamide	7.85	/	~0.75	~3.5	75% after 32000 s	[50]
Pyrolysis at 900 °C	3-aminopropyltriethoxysilane (AMPTS)	2.92	SiO_2/Etched by HF and HCl	0.973	7.154	Not shown	[51]
CVD at 800 °C	Pyridine	5.0	Ni/Etched by HCl	1.05	~6.8	94% after 7 days	[52]
Pyrolysis at 900 °C	GO, $[Bmim]BF_4$	6.6	/	0.89	3.69	Almost 100% after 18000 s	This work

[a]Conversion of different reference electrodes into RHE [53]:
$E_{vs.RHE}=E_{vs.Ag/AgCl}+ E°_{vs.Ag/AgCl}+0.059pH$(at 298 K)
$E_{vs.RHE}=E_{vs.Hg/HgO}+ E°_{vs.Hg/HgO}+0.059pH$(at 298 K)
[b]Current density refers to data collected at +0.3 V (vs. RHE) at 1600 rpm in RDE test.

4.3. Density functional theory (DFT) Analysis

DFT calculations were carried out to investigate the influence of different N configurations in N-doped graphene on the ORR performance enhancement. Three possible active configurations, namely, pyridinic N, pyrrolic N and graphitic N, were investigated.

Since the N atom in each of the three circumstances could be located either inside or at the edge of graphene, there were essentially six cases to be considered: Graphitc N-inside, Graphitic N-edge, Pyridinic N-inside, Pyridinic N-edge, Pyrrolic N-inside and Pyrrolic N-edge (Fig. S7). However, since the configuration of Pyrrolic N-inside was found to be unstable based on molecular structure optimization, only the remaining five cases were investigated. According to previous works [18, 23], either one of the following two requirements has to be met for the atoms to be ORR active sites: (1) large positive spin density; (2) small absolute value of the negative spin density and large charge density. Our computational results show that after N doping, there are significant changes in both the charges and the spins of some of the atoms. For instance, the positive charges and spins of some atoms can reach as high as around 0.19. In this work, we set the cutoff for large atomic charges and atomic spins as those with the values larger than 0.1.

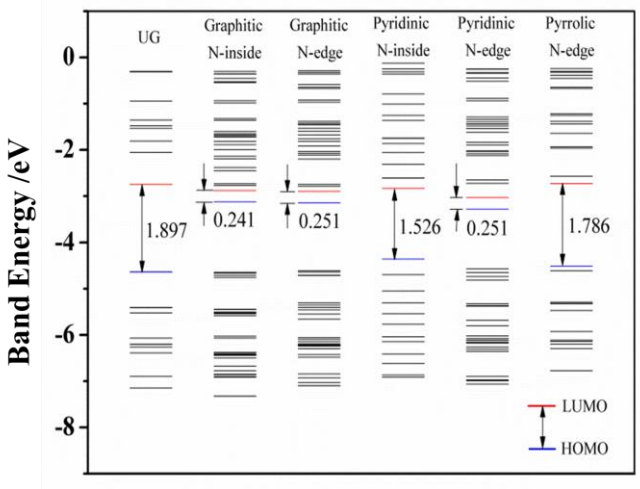

Fig. 6. Molecular orbital energy profile diagram of UG and N-doped graphene with different N configurations.

The highest-occupied molecular orbital (HOMO) and lowest-unoccupied molecular orbital (LUMO) energy of these systems were obtained to calculate the energy gap. A small HOMO-LUMO gap implies low kinetic stability and high chemical reactivity. Molecular orbital energy profile diagram and the HOMO-LUMO energy gap of different systems are

illustrated in Fig. 6. The replacement of C with N results in the decrement of the energy gap, which is especially significant for the systems of Graphitic N-inside, Graphitic N-edge, and Pyridinic N-edge, changing from 1.897 eV of UG to around 0.24 eV to 0.25 eV.

The atoms that are likely to act as ORR active sites are presented in Fig. 7 and Table 3. No ORR active site is found in UG since the atomic charges are small and the spin density is 0 for all atoms. On the other hand, there are five active sites in Graphitic N-inside, three of which, including the N atom, have the spins larger than 0.1. The other two show small spins but large charges, which makes them the active atomic sites too. Four and eight possible active sites are identified in Graphitic N-edge and Pyridinic N-edge, respectively. Unlike Graphitic N-inside, the N atom in Graphitic N-edge has no catalytic activity. The N in Graphitic N-edge shows a small charge and spin of 0.018 and 0.085, respectively. The N in Pyridinic N-edge has a large spin density of 0.1155, making it very likely to be an ORR active site. For Pyridinic N-inside and Pyrrolic N-edge, there are only two active sites with a large charge resulting from the large electronegativity of N. On the other hand, the spins of atoms are nearly zero owing to the even number of electrons in these two systems.

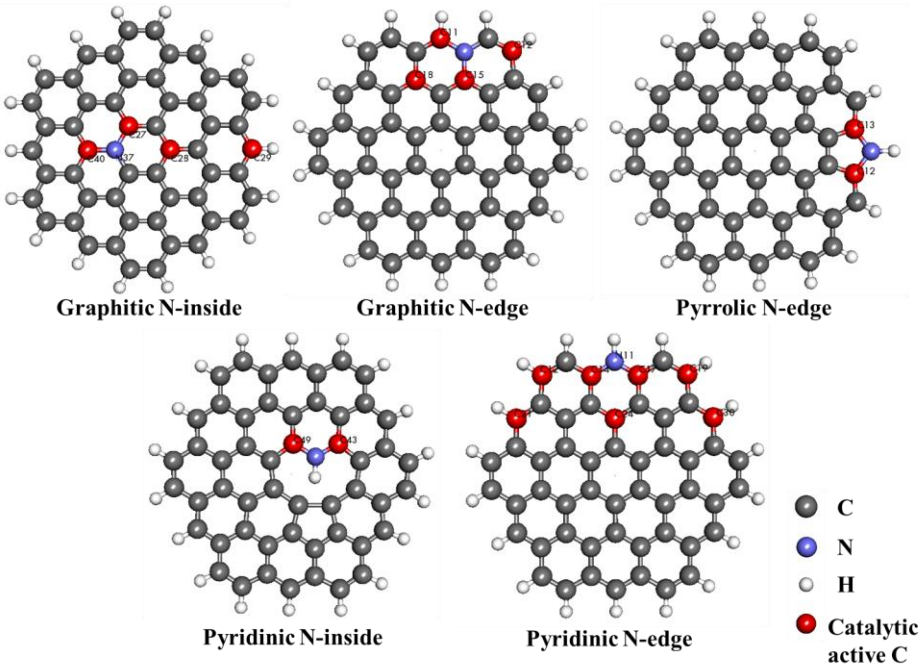

366

367 **Fig. 7.** Distribution of possible ORR catalytic active sites on the N-doped graphene with different N

368 configurations based on the DFT calculations.

369

370

371

63

64

65

Table 3. Atomic charge and spin of the catalytic active sites in the N-doped graphene with different N configurations.

N Configuration	Atoms No.	Atomic Charge	Atomic Spin
Pyridinic N-edge	N11	-0.2365	0.1155
	C12	-0.1292	0.1025
	C14	0.1539	0.0666
	C17	0.1539	0.0666
	C19	-0.1292	0.1025
	C21	-0.1442	0.1004
	C24	0.0345	0.1071
	C30	-0.1442	0.1005
Graphitic N-inside	C27	0.1295	0.0687
	C28	0.0265	0.1191
	C29	-0.1583	0.1594
	C40	0.1475	-0.0095
	N37	-0.0095	0.1102
Graphitic N-edge	C11	-0.0842	0.1920
	C12	-0.1642	0.1014
	C15	0.1325	0.0312
	C18	0.0264	0.1128
Pyridinic N-inside	C43	0.1754	-0.0010
	C49	0.1777	-0.0007
Pyrrolic N-edge	C12	0.1425	-0.0006
	C13	0.1425	-0.0006

All in all, among the five N doping configurations considered here, Pyridinic N-edge is the most favorable configuration for ORR considering that it has the largest number of active sites (eight in total) as well as the remarkable reduction of the energy gap to 0.251 eV. Pyridinic N-inside and Pyrrolic N-edge show the poorest ORR catalytic activity since they have only two active sites and the large HOMO-LUMO energy gaps also make them less

active. The ORR catalytic activity of Graphitic N-inside and Graphitic N-edge is in between those two groups with five and four active sites, respectively. This is well consistent with previous works and our experimental results, in which NG900 with a high proportion of pyridinic N and graphitic N exhibits the best catalytic performance towards ORR [49, 54]. Although NG1000 has an even higher ratio of active N configurations, the low N doping content and severe morphology change resulting from the high temperature lead to the poor ORR catalytic performance.

5. Conclusions

A facile and environmental-friendly method has been developed for synthesis of high-quality N-doped graphene by calcination of uniform mixture of graphene oxide (GO) and traditional hydrophilic ionic liquid 1-butyl-3-methylimidazolium tetrafluoroborate ([Bmim]BF_4) which serves as both N source and restacking protectant. The calcination temperature has profound effect on the chemical composition and microstructure of the as-obtained catalysts. The catalyst prepared at 900 ℃ with N doping content of 6.6 at% exhibits the highest catalytic performance towards oxygen reduction reaction (ORR) in alkaline condition. Calculations based on density functional theory (DFT) indicate that pyridinic N locating at the edge of graphene is the most active configuration for ORR owing to the largest number of active sites and lower band gap. Hence, the ORR catalytic activity enhancement of N-doped graphene in this work can be ascribed to the superior electronic conductivity of graphene, the high N doping content and the high proportion of active pyridinic N moieties. This paper not only presents a facile, green and scalable way to synthesize N-doped graphene which is a highly cost-effective catalyst for fuel cell and metal-air battery, but also gives valuable insights from the atomic point of view into the structure-property relationships of N-doped graphene towards ORR.

Acknowledgements

This research was supported by the Hong Kong General Research Fund (GRF CityU 11207414) and CityU Strategic Research Grant (Projects 7004689 and 7004923). We also gratefully acknowledge the financial support from the National Natural Science Foundation of China (No. 51364007, No. 21001117), the Natural Science Foundation of Shenzhen (Basic Research, JCYJ20150331101823677 and JCYJ20160428154632404), the Shenzhen Peacock Plan (KQCX20140522150815065), the Starting-Up Funds of South University of Science and Technology of China (SUSTC) through the talent plan of the Shenzhen Government, the Science and Technology Innovation Foundation for the Undergraduates of SUSTC (2014S07, 2015X19), the CityU Start-up Grant (No. 7200397), and the CityU SRG Fund (No. 7004166).

Appendix A. Supplementary Information

Supplementary data associated with this article can be found, in the online version, at .

References

[1] Buller S, Strunk J. Nanostructure in energy conversion. J Energy Chem 2016;25:171-90.
[2] Zhao C-e, Gai P, Song R, Chen Y, Zhang J, Zhu J-J. Nanostructured material-based biofuel cells: recent advances and future prospects. Chem Soc Rev 2017;46:1545-64.
[3] Frattini D, Accardo G, Ferone C, Cioffi R. Fabrication and characterization of graphite-cement composites for microbial fuel cells applications. Mater Res Bull 2017;88:188-99.
[4] Tan P, Chen B, Xu HR, Zhang HC, Cai WZ, Ni M, et al. Flexible Zn- and Li-air batteries: recent advances, challenges, and future perspectives. Energy Environ Sci 2017;10:2056-80.
[5] Li L, Fan W, Xuan J, Leung MKH, Zheng K, She Y. Optimal design of current collectors for microfluidic fuel cell with flow-through porous electrodes: Model and experiment. Appl Energy 2017;206:413-24.
[6] Pei P, Wang K, Ma Z. Technologies for extending zinc–air battery's cyclelife: A review. Appl Energy 2014;128:315-24.
[7] Tan P, Shyy W, Zhao TS, Zhang RH, Zhu XB. Effects of moist air on the cycling performance of non-aqueous lithium-air batteries. Appl Energy 2016;182:569-75.

[8] Banham D, Ye S, Pei K, Ozaki J-i, Kishimoto T, Imashiro Y. A review of the stability and durability of non-precious metal catalysts for the oxygen reduction reaction in proton exchange membrane fuel cells. J Power Sources 2015;285:334-48.
[9] Zhang C, Mahmood N, Yin H, Liu F, Hou Y. Synthesis of Phosphorus‐Doped Graphene and its Multifunctional Applications for Oxygen Reduction Reaction and Lithium Ion Batteries. Adv Mater 2013;25:4932-7.
[10] Jin J, Pan F, Jiang L, Fu X, Liang A, Wei Z, et al. Catalyst-Free Synthesis of Crumpled Boron and Nitrogen Co-Doped Graphite Layers with Tunable Bond Structure for Oxygen Reduction Reaction. ACS Nano 2014;8:3313-21.
[11] Qu K, Zheng Y, Dai S, Qiao SZ. Graphene oxide-polydopamine derived N, S-codoped carbon nanosheets as superior bifunctional electrocatalysts for oxygen reduction and evolution. Nano Energy 2016;19:373-81.
[12] Duan J, Chen S, Jaroniec M, Qiao SZ. Heteroatom-Doped Graphene-Based Materials for Energy-Relevant Electrocatalytic Processes. ACS Catal 2015;5:5207-34.
[13] ElMekawy A, Hegab HM, Losic D, Saint CP, Pant D. Applications of graphene in microbial fuel cells: The gap between promise and reality. Renewable Sustainable Energy Rev 2017;72:1389-403.
[14] Zhang J, Dai L. Heteroatom-Doped Graphitic Carbon Catalysts for Efficient Electrocatalysis of Oxygen Reduction Reaction. ACS Catal 2015;5:7244-53.
[15] Zhao J, Cabrera CR, Xia Z, Chen Z. Single−sided fluorine–functionalized graphene: A metal–free electrocatalyst with high efficiency for oxygen reduction reaction. Carbon 2016;104:56-63.
[16] Zhang J, Zhao Z, Xia Z, Dai L. A metal-free bifunctional electrocatalyst for oxygen reduction and oxygen evolution reactions. Nat Nanotechnol 2015;10:444.
[17] Gong K, Du F, Xia Z, Durstock M, Dai L. Nitrogen-Doped Carbon Nanotube Arrays with High Electrocatalytic Activity for Oxygen Reduction. Science 2009;323:760-4.
[18] Zhang L, Xia Z. Mechanisms of Oxygen Reduction Reaction on Nitrogen-Doped Graphene for Fuel Cells. J Phys Chem C 2011;115:11170-6.
[19] Zhang L, Niu J, Dai L, Xia Z. Effect of Microstructure of Nitrogen-Doped Graphene on Oxygen Reduction Activity in Fuel Cells. Langmuir 2012;28:7542-50.
[20] Li M, Zhang L, Xu Q, Niu J, Xia Z. N-doped graphene as catalysts for oxygen reduction and oxygen evolution reactions: Theoretical considerations. J Catal 2014;314:66-72.

[21] Lai L, Potts JR, Zhan D, Wang L, Poh CK, Tang C, et al. Exploration of the active center structure of nitrogen-doped graphene-based catalysts for oxygen reduction reaction. Energy Environ Sci 2012;5:7936-42.
[22] Zhou X, Tang S, Yin Y, Sun S, Qiao J. Hierarchical porous N-doped graphene foams with superior oxygen reduction reactivity for polymer electrolyte membrane fuel cells. Appl Energy 2016;175:459-67.
[23] Liang J, Jiao Y, Jaroniec M, Qiao SZ. Sulfur and Nitrogen Dual-Doped Mesoporous Graphene Electrocatalyst for Oxygen Reduction with Synergistically Enhanced Performance. Angew Chem Int Ed 2012;51:11496-500.
[24] Lee S, Choun M, Ye Y, Lee J, Mun Y, Kang E, et al. Designing a Highly Active Metal‐Free Oxygen Reduction Catalyst in Membrane Electrode Assemblies for Alkaline Fuel Cells: Effects of Pore Size and Doping-Site Position. Angew Chem Int Ed 2015;54:9230-4.
[25] Yang S, Peng L, Huang P, Wang X, Sun Y, Cao C, et al. Nitrogen, Phosphorus, and Sulfur Co-Doped Hollow Carbon Shell as Superior Metal-Free Catalyst for Selective Oxidation of Aromatic Alkanes. Angew Chem Int Ed 2016;55:4016-20.
[26] Lee MS, Choi H-J, Baek J-B, Chang DW. Simple solution-based synthesis of pyridinic-rich nitrogen-doped graphene nanoplatelets for supercapacitors. Appl Energy 2017;195:1071-8.
[27] Wu M, Zhang E, Guo Q, Wang Y, Qiao J, Li K, et al. N/S-Me (Fe, Co, Ni) doped hierarchical porous carbons for fuel cell oxygen reduction reaction with high catalytic activity and long-term stability. Appl Energy 2016;175:468-78.
[28] Lee JS, Wang X, Luo H, Baker GA, Dai S. Facile Ionothermal Synthesis of Microporous and Mesoporous Carbons from Task Specific Ionic Liquids. J Am Chem Soc 2009;131:4596-7.
[29] Yang W, Fellinger T-P, Antonietti M. Efficient Metal-Free Oxygen Reduction in Alkaline Medium on High-Surface-Area Mesoporous Nitrogen-Doped Carbons Made from Ionic Liquids and Nucleobases. J Am Chem Soc 2011;133:206-9.
[30] Sa YJ, Park C, Jeong HY, Park SH, Lee Z, Kim KT, et al. Carbon Nanotubes/Heteroatom‐Doped Carbon Core-Sheath Nanostructures as Highly Active, Metal-Free Oxygen Reduction Electrocatalysts for Alkaline Fuel Cells. Angew Chem Int Ed 2014;126:4186-90.
[31] Lee JS, Wang X, Luo H, Dai S. Fluidic Carbon Precursors for Formation of Functional Carbon under Ambient Pressure Based on Ionic Liquids. Adv Mater 2010;22:1004-7.

[32] Fechler N, Fellinger TP, Antonietti M. “Salt Templating”: A Simple and Sustainable Pathway toward Highly Porous Functional Carbons from Ionic Liquids. Adv Mater 2013;25:75-9.
[33] Wang X, Dai S. Ionic Liquids as Versatile Precursors for Functionalized Porous Carbon and Carbon–Oxide Composite Materials by Confined Carbonization. Angew Chem Int Ed 2010;49:6664-8.
[34] Yang W, Yue X, Liu X, Zhai J, Jia J. IL-derived N, S co-doped ordered mesoporous carbon for high-performance oxygen reduction. Nanoscale 2015;7:11956-61.
[35] She Y, Lu Z, Ni M, Li L, Leung MKH. Facile Synthesis of Nitrogen and Sulfur Codoped Carbon from Ionic Liquid as Metal-Free Catalyst for Oxygen Reduction Reaction. ACS Appl Mater Interfaces 2015;7:7214-21.
[36] Hummers WS, Offeman RE. Preparation of Graphitic Oxide. J Am Chem Soc 1958;80:1339.
[37] Wang S, Yu D, Dai L. Polyelectrolyte Functionalized Carbon Nanotubes as Efficient Metal-free Electrocatalysts for Oxygen Reduction. J Am Chem Soc 2011;133:5182-5.
[38] Perdew JP, Burke K, Ernzerhof M. Generalized Gradient Approximation Made Simple. Phys Rev Lett 1996;77:3865-8.
[39] Vanderbilt D. Soft self-consistent pseudopotentials in a generalized eigenvalue formalism. Phys Rev B 1990;41:7892-5.
[40] Paolo G, Stefano B, Nicola B, Matteo C, Roberto C, Carlo C, et al. QUANTUM ESPRESSO: a modular and open-source software project for quantum simulations of materials. J Phys: Condens Matter 2009;21:395502.
[41] Wang S, Zhang L, Xia Z, Roy A, Chang DW, Baek JB, et al. BCN Graphene as Efficient Metal‐Free Electrocatalyst for the Oxygen Reduction Reaction. Angew Chem Int Ed 2012;51:4209-12.
[42] Cui Z, Wang S, Zhang Y, Cao M. A simple and green pathway toward nitrogen and sulfur dual doped hierarchically porous carbons from ionic liquids for oxygen reduction. J Power Sources 2014;259:138-44.
[43] Tamboli SH, Kim BS, Choi G, Lee H, Lee D, Patil UM, et al. Post-heating effects on the physical and electrochemical capacitive properties of reduced graphene oxide paper. J Mater Chem A 2014;2:5077-86.
[44] Fei H, Dong J, Arellano-Jiménez MJ, Ye G, Dong Kim N, Samuel ELG, et al. Atomic cobalt on nitrogen-doped graphene for hydrogen generation. Nat Commun 2015;6:8668.

[45] Zhang J, Li C, Peng Z, Liu Y, Zhang J, Liu Z, et al. 3D free-standing nitrogen-doped reduced graphene oxide aerogel as anode material for sodium ion batteries with enhanced sodium storage. Sci Rep 2017;7:4886.
[46] Geng D, Chen Y, Chen Y, Li Y, Li R, Sun X, et al. High oxygen-reduction activity and durability of nitrogen-doped graphene. Energy Environ Sci 2011;4:760-4.
[47] Wang X, Wang J, Wang D, Dou S, Ma Z, Wu J, et al. One-pot synthesis of nitrogen and sulfur co-doped graphene as efficient metal-free electrocatalysts for the oxygen reduction reaction. Chem Commun 2014;50:4839-42.
[48] Sharifi T, Hu G, Jia X, Wågberg T. Formation of Active Sites for Oxygen Reduction Reactions by Transformation of Nitrogen Functionalities in Nitrogen-Doped Carbon Nanotubes. ACS Nano 2012;6:8904-12.
[49] Guo D, Shibuya R, Akiba C, Saji S, Kondo T, Nakamura J. Active sites of nitrogen-doped carbon materials for oxygen reduction reaction clarified using model catalysts. Science 2016;351:361-5.
[50] Zhang Y, Fugane K, Mori T, Niu L, Ye J. Wet chemical synthesis of nitrogen-doped graphene towards oxygen reduction electrocatalysts without high-temperature pyrolysis. J Mater Chem 2012;22:6575-80.
[51] Tang S, Zhou X, Xu N, Bai Z, Qiao J, Zhang J. Template-free synthesis of three-dimensional nanoporous N-doped graphene for high performance fuel cell oxygen reduction reaction in alkaline media. Appl Energy 2016;175:405-13.
[52] Ito Y, Qiu HJ, Fujita T, Tanabe Y, Tanigaki K, Chen M. Bicontinuous Nanoporous N‐doped Graphene for the Oxygen Reduction Reaction. Adv Mater 2014;26:4145-50.
[53] Liang H-W, Zhuang X, Brüller S, Feng X, Müllen K. Hierarchically porous carbons with optimized nitrogen doping as highly active electrocatalysts for oxygen reduction. Nat Commun 2014;5:4973.
[54] Sharma PP, Wu J, Yadav RM, Liu M, Wright CJ, Tiwary CS, et al. Nitrogen-Doped Carbon Nanotube Arrays for High‐Efficiency Electrochemical Reduction of CO2: On the Understanding of Defects, Defect Density, and Selectivity. Angew Chem Int Ed 2015;54:13701-5.